Reverse Intermodulation in Multi-Tone Array Transmitters

Anton N. Atanasov[#1], Mark S. Oude Alink[#], Frank E. van Vliet[*#]
[#]Integrated Circuit Design, University of Twente
[*]Defence, Safety & Security, TNO
[1]a.n.atanasov@utwente.nl

***Abstract*— The modern spectral, and thereby linearity, requirements force 5G phased-array transmitter systems to operate at reduced power efficiency, as they can no longer use voluminous filtering. To reduce the linearity requirements of the transmitter, we consider the case of an array consisting of closely spaced radiating elements operating at different frequencies. The coupled tones from one element to another create reverse intermodulation distortion (RIMD). We explain how RIMD is created within a power amplifier (PA), and derive an estimate for the power of the RIMD components. We provide a set of measurements for an X-Band GaAs PA and draw a direct comparison between RIMD and IMD. We show that RIMD has a third-order behaviour up to very high reverse power levels, opening up the perspective for higher output power operation as well as simpler and lower-power predistortion in multi-tone array systems such as 5G and radar.**

***Keywords*— interleaved arrays, reverse intermodulation, power amplifiers, intermodulation, nonlinearity, transmitters**

I. Introduction

The introduction of 5G brings new spectral challenges, limiting phased-array transmitters (TX) to operate at reduced power efficiency. Each individual frequency band will require a separate, and possibly adaptive, filter. Additionally, Multiple-Input Multiple-Output (MIMO) systems also introduce specific filter requirements, completely foregoing the possibility to use voluminous filtering. This leads to even more demanding power amplifier (PA) specifications.

Reverse Intermodulation Distortion (RIMD) occurs when signals from one transmitter couple to the output ports of nearby TXs and vice-versa, with the coupling strength being dependent on the type of elements used, their spacing and polarization. These reverse travelling signals mix in the output stage with the carrier frequency of the victim's PA, producing intermodulation components akin to regular intermodulation distortion (IMD) [1], as illustrated in Figure 1, where Ψ_1 and Ψ_2 are two distinct frequencies, both within the bandwidth of the PA. This phenomenon is becoming increasingly relevant in high density and high linearity systems such as radar and 5G. Particularly active arrays cannot make use of voluminous filtering, making RIMD more of a concern.

The problem of RIMD has been identified by the telecommunications and defense industries [2]–[4], being a subset of the broader problem of jamming, and respective standards have been created. The ETSI EN 300086 standard [5] introduces intermodulation attenuation, which is the ability of a PA to resist generating RIMD components in the presence of an interfering signal at its output. The standard also provides a measurement setup, however it does not specify any acceptable limits. Additionally, ITU has presented the same metric as intermodulation conversion loss [6], also without defining limits to these effects.

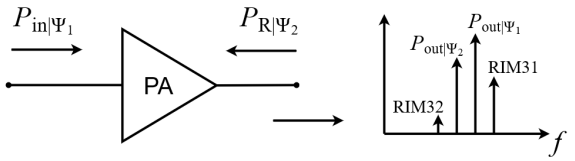

Fig. 1. Illustration of the RIMD effect. The signals $P_{\text{in}|\Psi_1}$ and $P_{\text{R}|\Psi_2}$ mix in the PA, resulting in a polluted output spectrum.

In this work we consider a relationship between the power of RIMD and IMD components of a PA within the context of a phased-array system operating at multiple signals, such as a densely interleaved array (DIA) system [7] in which the decreased antenna element spacing and different operating tones lead to an increase in RIMD. While IMD measurements are widely available, measuring RIMD is challenging due to the high power levels injected at the output of a PA. For a quick assessment, or for an assessment where a proper RIMD measurement setup is not available, the RIMD estimator can be very handy. In combination with an actual RIMD measurement setup, this RIMD estimator may provide valuable insight for tracing back the cause of the RIMD.

In Section II a relationship is derived between the strengths of the IMD and the RIMD components. Based on the relationship we derive an RIMD estimate for when the PA operates in compression. In Section III the IMD and RIMD components are measured on an X-band GaAs PA and are used to confirm the predictions. Finally, the conclusions are summarized in Section IV.

II. Analysis of Reverse IMD

Both ETSI [5] and ITU [6] model the mechanism of RIMD as a form of conversion loss, based on the assumption that the generated RIMD power is much less than the incoming interference power. Such a definition is vague, and without a metric for RIMD we can neither state limits for a given transmitter system, nor develop insights for reducing the effect. This is particularly important in the case of an antenna array,

where the load impedance Z_{L} is a function of the scan angle and all other phase modulations, leading to reflections for both the output power $P_{\mathrm{out}|\Psi_1}$ and the reverse power $P_{\mathrm{R}|\Psi_2}$.

There are two special cases when a PA experiences RIMD. In the first case, when $\Psi_1 = \Psi_2$, the system reduces to the well-known active load-pull configuration, given that the signals' magnitude and phase are controlled. In the second case, when $\Psi_1 \neq \Psi_2$ we become interested only in the amplitude of the RIMD components, as there is, in general, no phase relationship between the tones. It has been shown that RIMD is a function of odd-order harmonics [1] in addition to being dependent on the technology [8] and topology [9] of the PA. There are indications this RIMD mechanism applies to GaN, CMOS and GaAs based PAs [10]–[13]. We choose to draw a comparison between the power of the RIMD and IMD components and make the assumption that both of them are governed by similar weakly-nonlinear mechanisms.

The IMD components are generated by having one applied input power, $P_{\mathrm{in}|\Psi_1}$ fixed, while the other one, $P_{\mathrm{in}|\Psi_2}$, is varied. This results in an asymmetry in the IM3 components. The highest component, which we define as IM31, increases linearly with applied input power $P_{\mathrm{in}|\Psi_2}$ and has a slope of 1dB/dB, while the second component, IM32, is lower and grows at twice the rate with a slope of 2dB/dB. Similar behaviour is expected for the RIMD case, when $P_{\mathrm{R}|\Psi_2}$ is applied to the output, while the input power $P_{\mathrm{in}|\Psi_1}$ is again kept constant. We formulate this assumption in dB-scale as

$$P_{\mathrm{in}|\Psi_2} + G_{\mathrm{in}|\Psi_2} - \mathrm{IM31} \approx P_{\mathrm{R}|\Psi_2} + G_{\mathrm{R}|\Psi_2} - \mathrm{RIM31}, \quad (1)$$

where $G_{\mathrm{in}|\Psi_2}$ and $G_{\mathrm{R}|\Psi_2}$ are the gains, to be specified more clearly later on, toward the PA output for tones applied at the input and output, respectively, and under the condition that the input power $P_{\mathrm{in}|\Psi_1}$ is the same in both cases. If $P_{\mathrm{in}|\Psi_2} = P_{\mathrm{R}|\Psi_2}$, we define $\overline{\mathrm{RIM31}}$ as the dB-scale estimator for RIM31

$$\overline{\mathrm{RIM31}} \triangleq G_{\mathrm{R}|\Psi_2} - G_{\mathrm{in}|\Psi_2} + \mathrm{IM31}. \quad (2)$$

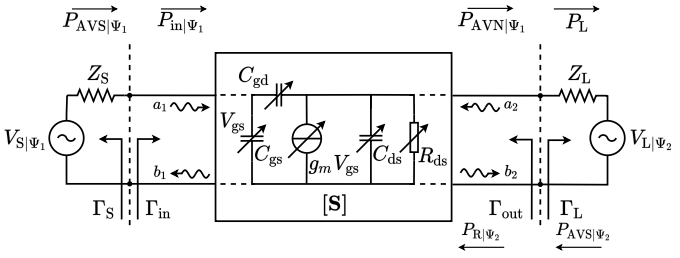

Fig. 2. Small signal representation of a simplified nonlinear transistor [14] inside a PA network with arbitrary impedances acting as either source or load for a given tone. The upper power references relate to the normal PA operation, while the bottom power references relate to the reverse power case.

To specify the precise definition of $G_{\mathrm{in}|\Psi_2}$ and $G_{\mathrm{R}|\Psi_2}$, we consider the general case of a two-port PA which transmits at Ψ_1 and receives reverse power at Ψ_2, as shown in Figure 2. The load impedance Z_{L} is different for each frequency, antenna pointing angle and includes all mutual coupling effects within the array.

For $G_{\mathrm{in}|\Psi_2}$, the two-port PA delivers power to the load Z_{L}. In this configuration the power gain G_{P}, available power gain G_{A} and transducer gain G_{T} are well known. For the sake of convenience when comparing RIMD to IMD, we are interested in working with a gain expression that is independent of Z_{L}. Of the three gain definitions, only the available power gain G_{A} meets the requirement and so we define

$$G_{\mathrm{in}|\Psi_2} \triangleq G_{\mathrm{A}} = \frac{|S_{21}|^2}{|1 - S_{11}\Gamma_{\mathrm{S}}|^2} \frac{1 - |\Gamma_{\mathrm{S}}|^2}{(1 - |\Gamma_{\mathrm{out}}|^2)}, \quad (3)$$

where

$$\Gamma_{\mathrm{out}} = S_{22} + \frac{S_{12}S_{21}\Gamma_S}{1 - S_{11}\Gamma_S} \quad (4)$$

and Γ_{S} is the source reflection coefficient.

For $G_{\mathrm{R}|\Psi_2}$, the impedance Z_{L} is part of a source and the two-port PA receives the reverse power $P_{\mathrm{R}|\Psi_2}$. Said power enters the system through a_2 (see Figure 2). We are interested in determining how much of that power is absorbed by the system and how much is reflected back to Z_{L} through b_2, irrespective of PA design. A metric which conveniently captures this relationship, and is independent of Z_{L}, is the output reflection coefficient and so

$$G_{\mathrm{R}|\Psi_2} \triangleq \frac{P_{\mathrm{AVN}}}{P_{\mathrm{R\text{-}in}}} = \frac{P_{\mathrm{L}}}{P_{\mathrm{R\text{-}AVS}}} = \left|\frac{b_2}{a_2}\right|^2 = |\Gamma_{\mathrm{out}}|^2. \quad (5)$$

Equations 5 and 3 are formulated such that they are independent of Z_L, making it applicable for every coupled signal in an array. Additionally, both G_{A} and $|\Gamma_{\mathrm{out}}|^2$ incorporate the output matching network's contribution. Thus our RIMD estimate for Equation 2 becomes

$$\overline{\mathrm{RIM31}} = |\Gamma_{\mathrm{out}}|^2 - G_{\mathrm{A}} + \mathrm{IM31}. \quad (6)$$

The main contributing factors are $|S_{21}|^2$ and $|S_{22}|^2$, thus the relationship in Equation 6 is valid only if the last stage of the PA is the dominant contributor of nonlinearity. Should a PA exhibit saturation at an earlier stage the above estimate will not hold. This opens the possibility of using Equation 6 to identify nonlinear contributions within multi-stage PA designs.

Naturally, there is a limit to the accuracy of the estimator depending on how representative the S-parameter measurements are, as they represent a linearization around a given bias point. This limits their accuracy for large voltage swings, e.g. above the compression point of the PA. We will show, however, that this is valid over a very wide and useful range.

III. Measurement of Reverse IMD and IMD

An X-Band XP1006 GaAs PA [15] is chosen as our device under test (DUT) for this study due to its wide use, making it a representative example. The XP1006's S-parameters are $|S_{11}|^2 \approx -15$dB, $|S_{21}|^2 \approx 24$dB, $|S_{12}|^2 \approx -54$dB and $|S_{22}|^2 \approx -12$dB in the band of interest from 9.5GHz to 10.5GHz. The $P_{0.1\mathrm{dB}}$, $P_{1\mathrm{dB}}$, $P_{3\mathrm{dB}}$ and $P_{6\mathrm{dB}}$ compression points are measured at about 2.1dBm, 6.5dBm, 10.2dBm and 15.2dBm, respectively.

A. Measurement Setup

Measurement of the RIMD behavior was done using the setup shown in Figure 3. The N5242B PNA-X microwave network analyzer connects to the DUT input directly, while an isolated CTT ASM/180 − 4040 driver PA is used to provide sufficient amplification to the reverse power, $P_{\mathrm{R}|\Psi_2}$, which is fed into the output of the DUT. The incoming and outgoing waves at the DUT's output are measured with the help of a directional coupler, protected with a 20dB attenuator on the driver PA side. The DUT is controlled by an IV Pulser using a 1ms pulse-width and a 5% duty-cycle. The output of the DUT is swept from 7.5 to 37dBm by $P_{\mathrm{R}|\Psi_2}$ fixed at 10GHz. At the same time the DUT is driven into its $[P_{0.1\mathrm{dB}}, P_{1\mathrm{dB}}, P_{3\mathrm{dB}}]$ compression points by $P_{\mathrm{in}|\Psi_1}$ for frequency offsets, Δ_f, of $[0.1, 1, 10, 100]$MHz above 10GHz.

The setup in Figure 3 is modified to measure the IMD behavior of the DUT. The driver PA is removed and the two signal generators, Source 1 and Source 2, are combined using an external diplexer. The power $P_{\mathrm{in}|\Psi_2}$ is swept from −10 to 10dBm at 10GHz, while the power $P_{\mathrm{in}|\Psi_1}$ is set to 10.2dBm for Δ_f of $[0.1, 1, 10, 100]$MHz above 10GHz. The compression level of the DUT, due to both input powers, ranges from a little over $P_{3\mathrm{dB}}$ to $P_{6\mathrm{dB}}$.

In all the measurements the PNA-X is set with an IF bandwidth of 1.5kHz, and the measurement is triggered to take place 100us after the RF pulse to avoid any transient effect of the DUT. Both the output and the input of the DUT are 50Ω matched.

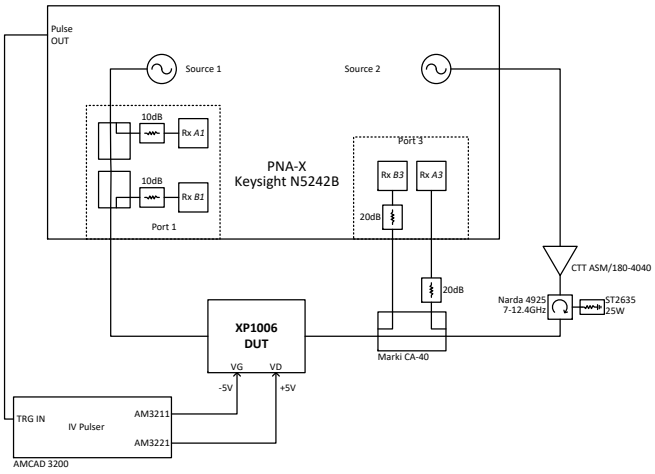

Fig. 3. The PNA-X drives the input of the XP1006 PA, while the output is modulated with the help of an isolated driver PA. A directional coupler is used to observe the incoming and outgoing waves at the PA's output. The PA is controlled by an IV Pulser.

B. Measurement Results

Figure 4a) shows the output spectrum of an RIMD measurement with $P_{\mathrm{R}|\Psi_2} = 7.5$dBm at 10GHz and $P_{\mathrm{in}|\Psi_1} = 10.2$dBm at 10.01GHz ($\Delta_f = 10$MHz). As $P_{\mathrm{R}|\Psi_2}$ increases, the strongest reverse intermodulation component, RIM31, located at 10.02GHz, increases linearly with a slope of 1dB/dB, while the second reverse intermodulation component, RIM32, increases with a slope of 2dB/dB, due to $P_{\mathrm{in}|\Psi_1}$ being constant. The RIMD components thus clearly show dominant third-order behavior. The measured output power is $P_{\mathrm{out}|\Psi_2} = -1.5$dBm, which tells us that $|\Gamma_{\mathrm{out}}|^2$, under large-signal conditions, is −9.2dB.

Figure 4b) shows the output spectrum of an IMD measurement with $P_{\mathrm{in}|\Psi_2} = 7.5$dBm at 10GHz and $P_{\mathrm{in}|\Psi_1} = 10.2$dBm at 10.01GHz ($\Delta_f = 10$MHz), and output powers $P_{\mathrm{out}|\Psi_1} = 29.2$dBm and $P_{\mathrm{out}|\Psi_2} = 25.3$dBm. Similar to the RIMD case, $P_{\mathrm{in}|\Psi_1}$ is kept constant, while $P_{\mathrm{in}|\Psi_2}$ is varied. This asymmetry in input power levels results in the IM3 components having the same slopes as those of the RIM3 components. The total input and output power levels are 15.0dBm and 33.5dBm, respectively. This gives us a gain of about 18.5dB, which is close to the $P_{6\mathrm{dB}}$ compression point of the DUT. In contrast to the RIMD behaviour, IMD contains many more odd-order components.

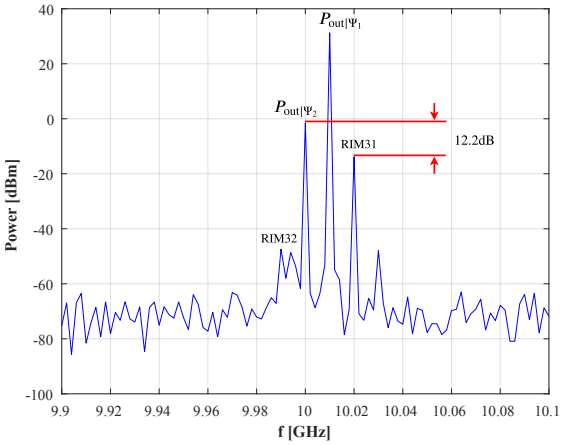

(a) Spectrum of RIMD measurement

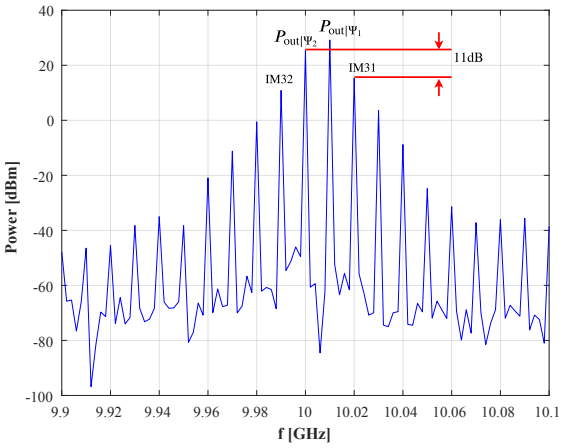

(b) Spectrum of IMD measurement

Fig. 4. Spectra of RIMD and IMD with $\Delta_f = 10$MHz, $P_{\mathrm{in}|\Psi_1} = 10.2$dBm and $P_{\mathrm{in}|\Psi_2} = P_{\mathrm{R}|\Psi_2} = 7.5$dBm.

Figure 5 plots $(\mathrm{RIM31} - P_{\mathrm{R}|\Psi_2})$ and $(\mathrm{IM31} - P_{\mathrm{in}|\Psi_2})$ as

a function of equal applied reverse and input power ($P_{\mathrm{R}|\Psi_2} = P_{\mathrm{in}|\Psi_2}$) at 10GHz, denoted as $P_{\mathrm{R=in}}$, with $P_{\mathrm{in}|\Psi_1} = 10.2$dBm and $\Delta_f = 10$MHz. The IM31 component, before the PA enters compression, is found to be 11.4dB higher than $P_{\mathrm{R=in}}$. For low $P_{\mathrm{R=in}}$ levels, the DUT operates around the P_{3dB} compression point, due to $P_{\mathrm{in}|\Psi_1}$. This results in $G_{\mathrm{A}} \approx 21.5$dB and so our estimate becomes $\overline{\mathrm{RIM31}} = -9.2 - 21.5 + 11.4 = -19.3$dB. The actual RIM31 component is found to be -21.5dB, which gives us an estimation error of 2.2dB.

As $P_{\mathrm{R=in}}$ increases to 10dBm, the IM31 component begins to enter strong compression. At that power level, the IM31 component itself is only 5dB higher than $P_{\mathrm{R=in}}$, which is a significant decrease. In this region the DUT operates at the P_{6dB} compression level and based on that $G_{\mathrm{A}} \approx 18.7$dB, which gives us $\overline{\mathrm{RIM31}} = -9.2 - 18.7 + 5 = -22.9$dB. The actual RIM31 component remains unchanged at -21.5dB, resulting in an estimation error of 1.4dB.

The estimation error ranges from 0.5 to 3.5dB for the other Δ_f offsets, with the largest error occuring at $\Delta_f = 100$kHz. The RIM31 component maintains a third-order behavior as $P_{\mathrm{R=in}}$ increases, eventually entering into compression at $P_{\mathrm{R=in}} \approx 32.5$dBm, which is comparable to the DUT's saturated output power level. This observation is in agreement with our assumption that the output nonlinearities affect both the IMD and RIMD effects in a similar way.

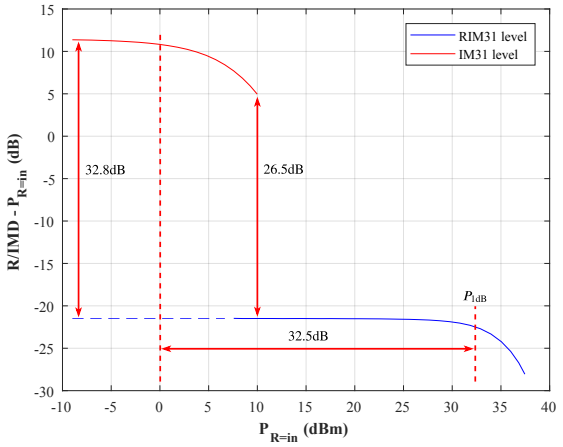

Fig. 5. Comparison between strongest IM3 and RIM3 components strength over equal applied input and reverse power $P_{\mathrm{R=in}}$ at 10GHz, $P_{\mathrm{in}|\Psi_1} = 10.2$dBm and $\Delta_f = 10$MHz.

IV. Conclusion

We have argued for the importance of RIMD in 5G and radar systems and the need to model its behavior, as it can give rise to incompatibility with radiated emission standards. We have shown that the RIM31 power, as a function of reverse power $P_{\mathrm{R}|\Psi_2}$, can be approximated as $|\Gamma_{\mathrm{out}}|^2 - G_A + \mathrm{IM31}$. The accuracy of the estimate, as measured on an XP1006 PA, varies from 0.5 to 3.5dB over several frequency offsets for high compression levels.

The weaker nature of RIMD relative to IMD allows for single-tone transmitters within a multi-tone system to operate at higher power levels and efficiency. As RIMD seems limited to third-order behaviour, even under full mutual coupling, our investigation opens the perspective for simpler and lower-power digital predistortion. Finally, the proposed method can be used to identify the source of non-linear contributions within a multi-stage PA design.

Acknowledgment

We would like to acknowledge Dr. Diogo Ribeiro from TNO for his help with measurements.

References

[1] E. Sinkevich and V. Mordachev, "Investigation of the transmitter susceptibility to reverse intermodulation by the use of double-frequency diagrams," in *2015 IEEE International Symposium on Electromagnetic Compatibility (EMC)*, Aug 2015, pp. 1159–1164.

[2] M. A. Maiuzzo and E. Mackouse, "Transmitter intermodulation product amplitudes," *1981 IEEE International Symposium on Electromagnetic Compatibility*, pp. 1–6, 1981.

[3] J. Gavan, "Analysis of intermodulation between broadband frequency transmitters on mobile radio networks," in *1982 IEEE International Symposium on Electromagnetic Compatibility*, Sep. 1982, pp. 1–7.

[4] F. German, K. Annamalai, M. Young, and M. C. Miller, "Simulation and data management for cosite interference prediction," in *2010 IEEE International Symposium on Electromagnetic Compatibility*, July 2010, pp. 869–874.

[5] ETSI, "Land Mobile Service Radio equipment with an internal or external RF connector intended primarily for analogue speech; Harmonised Standard covering the essential requirements of article 3.2 of the Directive 2014/53/EU," European Telecommunications Standards Institute, Tech. Rep. EN 300 086 V2.1.2, Aug. 2016.

[6] Radiocumminication Study Group 1, "Production and mitigation of intermodulation products in the transmitter," International Telecommunication Union, Tech. Rep. ITU-R SM.2021, 2000.

[7] A. Atanasov, M. S. Oude Alink, and F. E. van Vliet, "Densely interleaved arrays for dual-tone transmitters," in *Proc. IEEE Phase Array Systems and Technology (PAST'19)*, Boston, USA, Nov 2019, pp. 290–294.

[8] A. Katz, D. McGee, C. Brinton, and J. Qiu, "Sensitivity and Mitigation of Reverse IMD in power amplifiers," in *2011 IEEE Topical Conference on Power Amplifiers for Wireless and Radio Applications*, Jan 2011, pp. 53–56.

[9] M. Kamper, G. Ulbricht, R. Weigel, and G. Fischer, "Comparison of class A and class D RF amplifier operation with focus on reverse intermodulation and efficiency performance," in *2011 6th European Microwave Integrated Circuit Conference*, Oct 2011, pp. 272–275.

[10] A. Jarndal and A. Kouki, "Efficient modeling of GaN HEMTs for linear and nonlinear circuits design," *International Journal of Numerical Modelling: Electronic Networks, Devices and Fields*, vol. 30, no. 1, p. e2100, 2017.

[11] W. Cheng, A. J. Annema, J. A. Croon, D. B. M. Klaassen, and B. Nauta, "A general weak nonlinearity model for LNAs," in *2008 IEEE Custom Integrated Circuits Conference*, 2008, pp. 221–224.

[12] B. Raad, D. Sharma, K. Nigam, and P. Kondekar, "Physics-based simulation study of high-performance gallium arsenide phosphide–indium gallium arsenide tunnel field-effect transistor," *Micro Nano Letters*, vol. 11, no. 7, pp. 366–368, 2016.

[13] I. Angelov, M. Thorsell, M. Gavel, and O. Barrera, "On the modeling of high power FET transistors," in *2016 11th European Microwave Integrated Circuits Conference (EuMIC)*, Oct 2016, pp. 245–248.

[14] I. Angelov, L. Bengtsson, and M. Garcia, "Extensions of the chalmers nonlinear HEMT and MESFET model," *IEEE Transactions on Microwave Theory and Techniques*, vol. 44, no. 10, pp. 1664–1674, 1996.

[15] "XP1006 Datasheet," https://www.digchip.com/datasheets/parts/datasheet/1002/XP1006-FA.php.